Oral presentation | Mesh generation/adaptation
Mesh generation/adaptation-I
Wed. Jul 17, 2024 10:45 AM - 12:15 PM Room C

[7-C-02] Anisotropically Adapted Quad-dominant Meshes for High-order Discontinuous Galerkin Methods

*Dipendrasingh Kain[1], Gowri Venugopal[1], Aravind Balan[1], Ajay Rangarajan[2], Georg May[3] (1. Indian Institute of Sciecne (IISc), 2. RWTH Aachen University, 3. Von Karman Institute for Fluid Dynamics)

Keywords: Discontinuous Galerkin, Higher-order methods, Mesh adaptation , Metric-field , Compressible flows

Twelfth International Conference on
Computational Fluid Dynamics (ICCFD12),
Kobe, Japan, July 14-19, 2024

Anisotropically Adapted Quad-dominant meshes for High-order Discontinuous Galerkin Methods

D. Kain*, G. M. Venugopal*, A. Balan*, G. May** and A. Rangarajan***
Corresponding author: kains@iisc.ac.in
* Indian Institute of Science, Bengaluru, India.
** The von Karman Institute for Fluid Dynamics, Belgium.
*** RWTH Aachen University, Germany.

Abstract: Anisotropic meshes can simulate flows around aerospace vehicles more efficiently than isotropic meshes, as these flows are typically dominated by anisotropic features such as boundary layers and shocks. Metric field based methods provide a convenient framework for generating and manipulating anisotropic triangular meshes. The present work extends metric field based mesh adaptation for quad-dominant meshes for high-order Discontinuous Galerkin (DG) methods. Quads can better align the cell interfaces with shocks and boundary layers than triangular mesh, providing better accuracy than triangles for similar degrees of freedom. The solver used in the present study solves the governing equations on quad-dominant meshes. At a given adaptation cycle, the optimum metric field derived analytically is evaluated on the quad-dominant mesh. This metric field and the mesh obtained after splitting the quads into triangles are passed to a metric-conforming mesh generator to get the adapted triangular mesh. The triangular mesh is then recombined using the Blossom-Quad algorithm to get the adapted quad-dominant mesh. The blossom-quad algorithm based on perfect matching combines suitable triangles to give good quality quads. The entire framework is tested for scalar-advection diffusion test case and turbulent flow over a flat plate. The results show an optimum order of error convergence even on coarse meshes for the scalar case and faster drag convergence for the turbulent flat plate case.

Keywords: Mesh Adaptation, Metric field, Discontinuous Galerkin, Compressible flows, CFD

1 Introduction

According to the widely cited NASA's CFD Vision 2030 report, [1], mesh generation and adaptivity are significant bottlenecks in the current CFD workflow. Flows around aerospace vehicles often consist of complex phenomena at various length scales, such as boundary layers, shock waves, shock-boundary layer interactions, flow separation, etc. All flow features that affect the output must be resolved to obtain accurate functional output quantities like drag or lift. Uniformly refining the mesh is computationally expensive and impractical for flows around complex geometries. Mesh refinements based on some heuristics, such as refining regions with high gradients, offer an advantage over uniform refinement in terms of computational cost, but they may result in highly inaccurate solutions [2]. Manually generating meshes that are aligned with flow features such as shock waves or boundary layers is labor-intensive and only possible for simple test cases where the location of flow features is known a priori.

Realistic flows around aerospace vehicles often involve various anisotropic phenomena, which can be efficiently resolved through anisotropic mesh adaptation. Metric field based mesh adaptation provides a solid mathematical framework for anisotropic mesh adaptation [3]. The metric field embeds all information about simplicial (triangles in 2D and tetrahedras in 3D) mesh elements, i.e., their size, aspect ratio, and orientation. Hecht and Mohammad [4] showed that constructing a unit mesh in a given Riemannian metric space results in an anisotropic mesh in classical Euclidean space. Metric field based mesh adaptation has proven robust for 2D and 3D steady-state CFD simulations, generating highly anisotropic meshes around strong shocks and within the boundary layers [5]. Loseille et al. [6, 7] provide a detailed derivation of metric field based mesh adaptation for second-order finite volume methods. A great deal of metric field based mesh adaptation framework for second-order finite volume methods can be found in [8, 9, 10, 11 and 12]. High-order methods such as Discontinuous Galerkin (DG) offer superior accuracy compared to lower-order finite-volume methods at similar DoF, demonstrating exponential convergence in regions of smooth solutions. Dolejsi [13] derived a comprehensive framework for deriving metric fields for high-order hp-adaptive methods by minimizing interpolation error in Lq-norm. A detailed work on deriving metric fields for high-order methods can be found in [14, 15, 16, 17, 18, 19 and 20].

The methods mentioned above for deriving metric fields are robust and reliable for generating highly anisotropic unstructured meshes using simplicial elements near areas with shocks and boundary layers. However, the misalignment of mesh interfaces with shocks, boundary layers, and large dihedral angles negatively impacts solver stability and convergence speed, particularly for finite volume methods [21]. Candler et al. [22] demonstrated that such misalignment leads to significant entropy errors, propagating downstream and causing poor solution prediction near the body surface, and in some cases, resulting in carbuncle formation. On the other hand, a structured mesh (quads in 2D and hexahedra in 3D) can perfectly align with flow features, leading to faster numerical solvers and greater robustness. However, generating a structured mesh becomes challenging for complex geometries. A good compromise between structured and unstructured mesh is a hybrid mesh. A hybrid mesh featuring quads/hexes in the boundary layer and around shocks and triangles/tetrahedra elsewhere combines the advantages of structured mesh's high accuracy and robustness with the flexibility of mesh generation and adaptation found in unstructured meshes.

A widely used approach to generate nearly structured meshes within boundary layers and shock waves involves creating quasi-structured meshes with right-angled triangles in the regions exhibiting high anisotropy. These right-angled triangles are then combined into quads to create structured elements of high quality. Studies like [23, 24, 25, 26 and 27] have proven to be robust for generating quasi-structured meshes. In the present paper, we combine the mesh adaptation framework of [15] with the Blossom-Quad algorithm [28] to generate adapted quad-dominant meshes. Blossom-quad is an algorithm from the graph theory that computes the minimum cost perfect matching in a graph in polynomial time. This results in a combination of suitable triangles to get the most optimal quads of good quality. The methodology is validated with simple analytical test cases and turbulent flow over a flat plate.

The paper is organized as follows. Section 2 describes the metric-based mesh adaptation framework with a suitable error model and global optimization. Section 3 details the numerical test cases, and section 4 presents conclusions and future work.

2 Metric field based mesh Adaptation

2.1 Continuous mesh Model

Let $\mathcal{T}_h = \{\kappa\}$ be a triangulation of some computational domain $\Omega \subset \mathbb{R}^2$. Let vectors $\mathbf{e}_k$, for $k = 1, 2, 3$, denote the edges of the triangle. Then, for any nondegenerate triangle, there is a unique symmetric positive-definite matrix

$$\mathcal{M} = \begin{pmatrix} m_{11} & m_{12} \\ m_{12} & m_{22} \end{pmatrix}$$

such that, for a given constant $C > 0$.

$$\mathbf{e}_k^T \mathcal{M} \mathbf{e}_k = C, \quad k = 1, 2, 3 \tag{1}$$

Here, $\mathcal{M}$ is the (implied) metric tensor. The triangle is thus equilateral in the norm induced by the metric. A triangle that satisfies Eq. 1 and $C = 3$ can be inscribed in an ellipse E, with the ellipse's origin coinciding with the triangle's centroid, as shown in Fig. 1, is called a unit triangle. The spectral decomposition of $\mathcal{M}$ gives,

$$\mathcal{M} = Q_E \Lambda Q_E^T = \begin{pmatrix} \cos\theta & -\sin\theta \\ \sin\theta & \cos\theta \end{pmatrix} \begin{pmatrix} \lambda_1 & 0 \\ 0 & \lambda_2 \end{pmatrix} \begin{pmatrix} \cos\theta & -\sin\theta \\ \sin\theta & \cos\theta \end{pmatrix}^T \tag{2}$$

where Q_E is an orthogonal matrix whose columns are eigenvectors of $\mathcal{M}$, and Λ is a diagonal matrix containing eigenvalues of $\mathcal{M}$. The angle θ is the angle made by the major axis of E, with the positive x-axis as shown in Fig. 1. The relation between eigenvalues of $\mathcal{M}$ and the axis of an ellipse E, is $\lambda_i = \frac{1}{h_i^2}$, where h_1 and h_2 are the lengths of semi-minor and the major axis of ellipse respectively.

Using the duality between the ellipse E, and the inscribed unit triangle κ, we get the area of the triangle as,

$$|\kappa| = \frac{3\sqrt{3}}{4} h_1 h_2 = \frac{3\sqrt{3}}{4} \frac{1}{d} \tag{3}$$

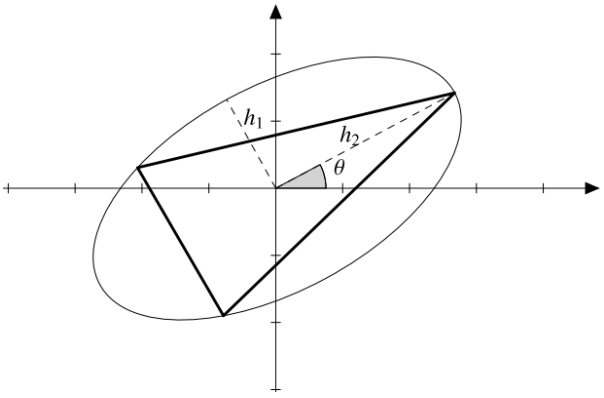

Figure 1: Choosing $C = 3$ in Eq. 1, a unit triangle w.r.t. $\mathcal{M}$ is inscribed in the ellipse $E := \{\mathbf{x} \in \mathbb{R}^2 : \mathbf{x}^T \mathcal{M} \mathbf{x} \leq 1\}$

where the local density is defined as $d = \sqrt{\lambda_1 \lambda_2} = \frac{1}{h_1 h_2} = \sqrt{det(\mathcal{M})}$. The aspect ratio of κ is defined as,

$$\beta = \sqrt{\frac{\lambda_1}{\lambda_2}} = \frac{h_2}{h_1} \geq 1 \tag{4}$$

Hence, a metric $\mathcal{M}$ can be defined by its anisotropy (β, θ) and its density (d). Thus, we can find a desired triangle by finding a metric with desired parameters (d, β, θ). A suitable error model is used to find a new discrete metric field. A metric-based mesh generator operates on a continuous metric field $(\mathcal{M}(x))_{x \in \Omega}$, which may be generated by a suitable interpolation of the new discrete metric field. Such a mesh generator will try to ensure that all edges of the triangulation are unit length w.r.t. to the new metric field. The length of a segment $\mathbf{e} = \mathbf{x}_2 - \mathbf{x}_1$ under the metric $\mathcal{M}(x)$ is defined using a straight line parameterization,

$$||\mathbf{e}||_{\mathcal{M}} = \int_0^1 \sqrt{\mathbf{e}^T \mathcal{M}(\mathbf{x}_1 + s\mathbf{e})e}\, ds \tag{5}$$

Practically a mesh generator tries to ensure $||\mathbf{e}||_M^2 \approx C$ in a least square sense. Hence, a discrete mesh is a snapshot of a continuous mesh, represented by a metric field $\mathcal{M}(x)$.

2.2 Error Model

From the previous section, it is evident that we can describe a local metric $\mathcal{M}$, corresponding to a triangle κ, by the tuple $(d_\kappa, \beta_\kappa, \theta_\kappa)_{\kappa \in \mathcal{T}_h}$. Thus, we need to construct a suitable error model that gives us the desired $(d_\kappa, \beta_\kappa, \theta_\kappa)$ based on the solution behavior in the domain. The error model minimizes the interpolation error in an approximation space given by,

$$V_{h,p} = \{v : v|_\kappa \in \mathcal{P}^p(\kappa), \forall \kappa \in \mathcal{T}_h\}, \tag{6}$$

where $\mathcal{P}^p$ is the space of polynomials of total degree at most p. If a p^{th} order polynomial is used to approximate the solution in a domian Ω, then the interpolation error is dominated by the $(p+1)^{st}$ term of the taylor series expansion. For a sufficiently smooth function u, at a point $\mathbf{x} = (x_1, x_2)^T \in \Omega$, and a polynomial degree p, the interpolation error $e_{\mathbf{x},p}(\mathbf{y})$ is given as,

$$|e_{\mathbf{x},p}(\mathbf{y})| \approx \frac{1}{(p+1)!} |u^{p+1,\phi}(\mathbf{x})||\mathbf{y} - \mathbf{x}|^{p+1}, \quad \forall \mathbf{y} \in \Omega \tag{7}$$

where, $u^{(k,\phi)}$ is a directional derivative of order k, defined as,

$$u^{(k,\phi)}(\mathbf{x}) = \sum_{l=0}^{k} \binom{k}{l} \frac{\partial^k u(\mathbf{x})}{\partial x_1^l \partial x_2^{k-l}} (\cos\phi)^l (\sin\phi)^{k-l}, \quad \phi \in [0, 2\pi) \tag{8}$$

To develop a suitable error model, we must approximate the error given by Eq. 7 by a 2×2 symmetric positive-definite matrix with only three unknowns. For $p = 1$, the metric would correspond to the hessian

of the solution variable, while for $p > 1$, there are increasingly many derivatives of order $p+1$, resulting in an overdetermined system. Dolejsi [13] derived a detailed framework, where the interpolation error given by Eq. 7 is bounded using three parameters (A_p, ρ_p, ϕ_p), such that for any $\mathbf{x} \in \Omega$, we have

$$|e_{\mathbf{x},p}(\mathbf{y})| \lesssim A_p \left((\mathbf{y}-\mathbf{x})^T Q_{\phi_p} D_{\rho_p} Q_{\phi_p}^T (\mathbf{y}-\mathbf{x}) \right)^{\frac{p+1}{2}}, \quad \forall \mathbf{y} \in \Omega \tag{9}$$

where,

$$Q_{\phi_p} = \begin{pmatrix} \cos\phi_p & -\sin\phi_p \\ \sin\phi_p & \cos\phi_p \end{pmatrix}, \quad D_{\rho_p} = \begin{pmatrix} 1 & 0 \\ 0 & \rho_p^{-\frac{2}{p+1}} \end{pmatrix}$$

and

$$\begin{aligned} A_p \equiv A_p(\mathbf{x}) &= \frac{1}{(p+1)!} |u^{(p+1,\phi_p)}(\mathbf{x})| \\ \phi_p \equiv \phi_p(\mathbf{x}) &:= \arg \max_{\phi \in [0,2\pi)} |u^{(p+1,\phi)}(\mathbf{x})| \end{aligned} \tag{10}$$

Let $\phi_p^\perp$ be the direction orthogonal to ϕ_p. Then, setting $A_p^\perp := |u^{(p+1,\phi_p^\perp)}(\mathbf{x})|$, we get

$$\rho_p \equiv \rho_p(\mathbf{x}) := \frac{A_p(\mathbf{x})}{A_p^\perp(\mathbf{x})} \tag{11}$$

It can be shown analytically that the bound given by Eq. 9 is guaranteed for $p = 1$, whereas for higher p, it is not guaranteed if the coefficients (A_p, ρ_p) are defined as in Eqs. 10 and 11. A numerical modification of the coefficients has been proposed in [13] to make the inequality in Eq. 9 safe (and sharp). However, we do not use this modification here because the benefit appears masked by other sources of error, such as the approximation of the higher-order derivatives. For a given area ν of the ellipse, we can determine the desired anisotropy parameters (β, θ) by minimizing the L^q-norm of the interpolation error given by Eq. 9 over an ellipse E

$$||e_{\mathbf{x},p}||_{L^q(E^*)} = \min_{|E|=\nu} ||e_{\mathbf{x},p}||_{L^q(E)} \tag{12}$$

The minimum is derived in [13] as,

$$\begin{aligned} ||e_{x,p}||_{L^q(E^*)} &\lesssim c_{p,q} A_p \rho_p^{-\frac{1}{2}} \nu^{\frac{p+1}{2}+\frac{1}{q}}, \\ c_{p,q}^q &= \frac{2}{q(p+1)+2} \pi^{\frac{-q(p+1)}{2}} \end{aligned} \tag{13}$$

The optimum is achieved for $\beta = \rho^{\frac{1}{p+1}}$ and $\theta = \phi_p - \frac{\pi}{2}$. The anisotropy parameters (β, θ) are thus eliminated and replaced by the higher derivatives of u via the parameters (A_p, ρ_p). Having fixed the optimized anisotropy, the size ν of the ellipse is still a free parameter. We use the global optimization approach of Rangarajan et al. [15] to get the optimum size distribution.

2.3 Global Optimization

Rangarajan et al. [15] proposed a continuous interpolation operator,

$$|e_\nu|(\mathbf{x}) := c_{p,q} A_p \rho_p^{-\frac{1}{2}} \nu^{\frac{p+1}{2}} \tag{14}$$

where the subscript ν indicates that the error still depends on area of ellipse. Combining Eqs. 13 and 14, we get

$$||e_{x,p}||_{L^q(E^*)}^q \lesssim e_\nu(\mathbf{x})^q \nu(\mathbf{x}) \tag{15}$$

For a triangle κ, centered at $\mathbf{x}_\kappa$, which is unit with respect to the metric $\mathcal{M}_\nu$, implied by the present (locally optimal) anisotropy and some arbitrary size ν. Then, $||e_{x_\kappa,p}||_{L^q(\kappa)} \lesssim ||e_{x_\kappa,p}||_{L^q(E^*)}$ with a constant that depends on the constant C in Eq. 1. Defining the interpolation operator π_h by a piecewise Taylor series, centered at each element centroid (i.e., $\pi_h|_\kappa = \pi_{x_\kappa,p}$, where $\pi_{x_\kappa,p}$ represents the Taylor

series of order p), one has

$$||u - \pi_h u||^q_{L^q(\Omega)} = \sum_{\kappa \in \mathcal{T}_h} ||u - \pi_{x_\kappa, p} u||^q_{L^q(\kappa)} \lesssim \sum_{\kappa \in \mathcal{T}_h} ||e(x_\kappa, p)||^q_{L^q(\kappa)} \lesssim \sum_{\kappa \in \mathcal{T}_h} e_\nu(\mathbf{x}_\kappa)^q \nu(\mathbf{x}) \tag{16}$$

where the last term can be thought of approximating the integral

$$\sum_{\kappa \in \mathcal{T}_h} e_\nu(\mathbf{x}_\kappa)^q \nu(\mathbf{x}) \sim \sum_{\kappa \in \mathcal{T}_h} e_\nu(\mathbf{x}_\kappa)^q |\kappa| \to \int_\Omega e_\nu(\mathbf{x}_\kappa)^q \, d\mathbf{x}, \quad (h \to 0) \tag{17}$$

The right-hand side of Eq. 17 defines our continuous mesh error model, which is thus seen to be asymptotically consistent with the error estimates derived in this section. The main advantage of representing the error model in a continuous form is that we can use powerful mathematical tools like calculus of variation to derive the distribution of element sizes analytically, given the number of elements as a constraint. Substituting $\nu = \pi h_1 h_2 = \pi/d$, we can rewrite error model from Eq. 14 in terms of continuous mesh density, $d \equiv d(\mathbf{x})$ as

$$|e_d|(\mathbf{x}) = \left(\frac{2}{q(p+1)+2} \right)^{1/q} A_p \rho_p^{-\frac{1}{2}} d^{-\frac{(p+1)}{2}} \tag{18}$$

Defining

$$E_{\mathcal{M}} := \int_\Omega |e_d|^q \, d\mathbf{x} = \int_\Omega \left(\frac{2}{q(p+1)+2} \right) \left(A_p \rho_p^{-\frac{1}{2}} \right)^q d^{-\frac{q(p+1)}{2}} \, d\mathbf{x} \tag{19}$$

we now consider the following constrained optimization problem:

$$d^\star = \arg\min_d E_{\mathcal{M}}, \quad \text{such that,} \quad N = \int_\Omega d \, d\mathbf{x} \tag{20}$$

Using the calculus of variations leads to the optimality condition,

$$\delta E_{\mathcal{M}} = -\left(\frac{q(p+1)}{q(p+1)+2} \right) \int_\Omega \left(A_p \rho_p^{-\frac{1}{2}} \right)^q d^{-\frac{q(p+1)+2}{2}} \delta d \, d\mathbf{x} = 0 \tag{21}$$

Taking a variation of the constraint equation (20), we have

$$\delta N = \int_\Omega \delta d \, d\mathbf{x} = 0 \tag{22}$$

Hence, an admissible solution to Eq. 21 is given by

$$\left(A_p \rho_p^{-\frac{1}{2}} \right)^q d^{-\frac{q(p+1)+2}{2}} = \text{const} \tag{23}$$

Solving for d from Eq. 23 and substituting the result into the constraint Eq. 20, we get,

$$d^\star(\mathbf{x}) = K \left(A_p(\mathbf{x}) \rho_p(\mathbf{x})^{-\frac{1}{2}} \right)^{\frac{2q}{q(p+1)+2}} \tag{24}$$

where

$$K = \frac{N}{\int_\Omega \left(A_p \rho_p^{-\frac{1}{2}} \right)^{\frac{2q}{q(p+1)+2}} \, d\mathbf{x}} \tag{25}$$

Substituting Eq. 25 into Eq. 24, we get the optimum density ($d^\star$) as,

$$d^\star(\mathbf{x}) = \frac{N \left(A_p \rho_p^{-\frac{1}{2}} \right)^{\frac{2q}{q(p+1)+2}}}{\int_\Omega \left(A_p \rho_p^{-\frac{1}{2}} \right)^{\frac{2q}{q(p+1)+2}} \, d\mathbf{x}} \tag{26}$$

The advantage of the above approach is that the only parameter to be set by the user is N, which is a continuous mesh equivalent to the total number of elements (n_h) in a triangulation ($\mathcal{T}_h$), of the domain

(Ω). In practical computations, the density (d) is computed as cell-wise constants only. Thus, Eq. 3 can be used to approximate N as follows:

$$N = \int_\Omega d\, d\mathbf{x} \approx \sum_{\kappa\in\mathcal{T}_h} \int_\kappa d_\kappa\, d\mathbf{x} = \sum_{\kappa\in\mathcal{T}_h} d_\kappa \int_\kappa d\mathbf{x} = \sum_{\kappa\in\mathcal{T}_h} d_\kappa |\kappa| = \sum_{\kappa\in\mathcal{T}_h} \frac{3\sqrt{3}}{4} \approx \frac{3\sqrt{3}}{4} n_h \tag{27}$$

Hence, one adaptation step consists of the following.

1. Compute the numerical solution of order p on a current quad-dominant mesh using any numerical method. Here, we have used the Hybridized Discontinuous Galerkin (HDG) method.
2. Calculate the directional derivatives of order $p+1$ from the current numerical solution. Compute the corresponding new anisotropy $(\beta_\kappa, \theta_\kappa)_{\kappa\in\mathcal{T}_h}$ in the form of (A_p, ρ_p).
3. Determine the new density of the mesh elements $d_\kappa = d^\star(\mathbf{x}_\kappa)$ for the desired mesh using Eq. 26. Calculate the new metric $(\mathbf{M}_\kappa)_{\kappa\in\mathcal{T}_h}$ from (A_p, ρ_p, d).
4. Split the quads of the current quad-dominant mesh to get a fully triangular mesh because a metric field based mesh generator works only on a triangular mesh.
5. This fully triangular mesh with the new metric $(\mathbf{M}_\kappa)_{\kappa\in\mathcal{T}_h}$ at its vertices are given as input to the metric field based mesh generator, which gives a new adapted triangular mesh. We have used BAMG [29] as a 2D mesh generator.
6. Use Blossom-Quad [28] algorithm to recombine triangles of new adapted mesh into quads to get an adapted quad-dominant mesh. This new quad-dominant mesh is used for the next computation.

3 Numerical Results

An in-house HDG solver has been used to carry out numerical simulations. The development of the solver was started by Woopen et al. [30], and the details regarding hybridization are given in [31]. The discretized nonlinear system resulting from HDG discretization is solved using the Newton-Raphson method. The linear subproblems from Newton-Raphson's method are solved using a restarted Generalized minimum residual method (GMRES) with Incomplete LU preconditioning.

3.1 Scalar Advection - Diffusion Test Case

Consider a scalar advection-diffusion equation with advection coefficient, $\beta = (1,1)^T$, and diffusion coefficient $\epsilon = 0.01$,

$$\begin{aligned} \beta\cdot\nabla u - \epsilon\nabla^2 u = s, \quad (x,y)\in\Omega = (0,1)^2, \quad \epsilon > 0 \\ u = 0, \quad (x,y)\in\partial\Omega \end{aligned} \tag{28}$$

Using method of manufactured solution, the source term s is set such that the exact solution $u(x,y)$ is given by,

$$u(x,y) = \left(x + \frac{e^{x/\epsilon}-1}{1-e^{1/\epsilon}}\right)\left(y + \frac{e^{y/\epsilon}-1}{1-e^{1/\epsilon}}\right) \tag{29}$$

The solution u exhibits a very strong boundary layer near $x=1$ and $y=1$. The smaller the diffusion coefficient (ϵ), the sharper the boundary layer. We solve Eq. 28 numerically, and assess the performance of the mesh adaptation framework based on the error between the numerical solution (u_h) and the exact solution (u), given by Eq. 29. We start with an initial coarse mesh with $n_h = 256$ elements, polynomial order $p=2$, and $DoF = 1440$. Fig. 2 shows the initial coarse mesh and the contour plot of the numerical solution. As seen from the contour plot, the initial mesh does not resolve the boundary layer accurately at the domain's top-right corner while the variation is captured accurately in the bottom-left region, where the solution varies almost quadratically. The L_2-norm of the exact error ($||u-u_h||_{L_2(\Omega)}$) on the initial mesh is 1.93×10^{-2}. The mesh is adapted by minimizing the interpolation error in the exact solution, i.e., using ($|e_{\mathbf{x},p}(\mathbf{y})| = |u-u_h|$) in Eq. 7. We obtain an adapted quad-dominant mesh at a given complexity N defined by Eq. 20. Fig. 3 shows the adapted quad-dominant mesh and the contour plot of the numerical solution with $n_h = 276$ elements, polynomial order $p=2$, and $DoF = 1479$. As

seen from Fig. 3, mesh elements are refined and highly anisotropic in the top-right corner of the domain, resolving the boundary layer accurately. Meanwhile, far away from the boundary layer, the elements are coarsened because a quadratically varying solution can be captured accurately even on coarse elements using $p = 2$ polynomial order. The L_2-norm of an exact error on an adapted mesh is 4.03×10^{-5}, which is three orders of magnitude less than the error on the initial mesh for almost the same DoF.

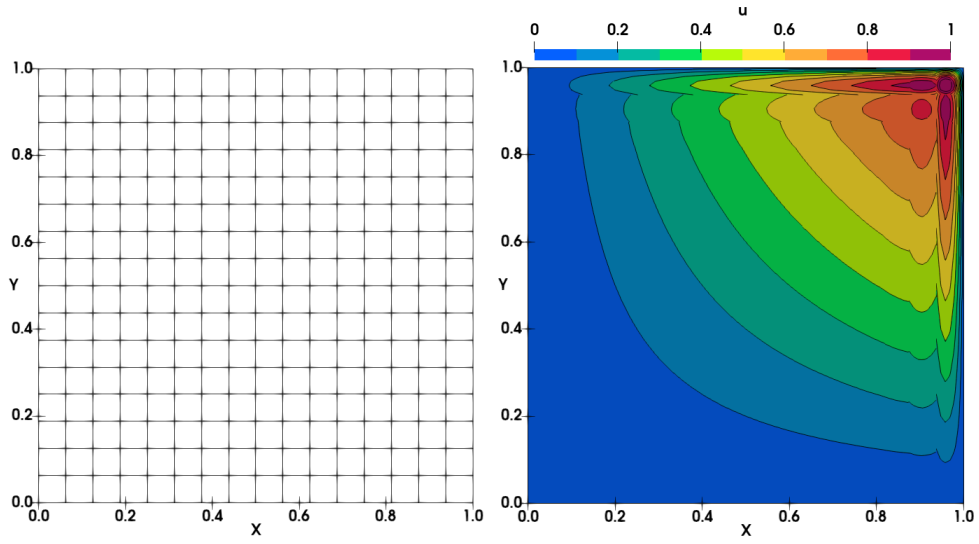

(a) (b)

Figure 2: Scalar Advection - Diffusion test case: (a) Initial mesh ($n_h = 256$, $DoF = 1440$, $p = 2$), (b) Contour plot of the numerical solution, $||u - u_h||_{L_2(\Omega)} = 1.93 \times 10^{-2}$

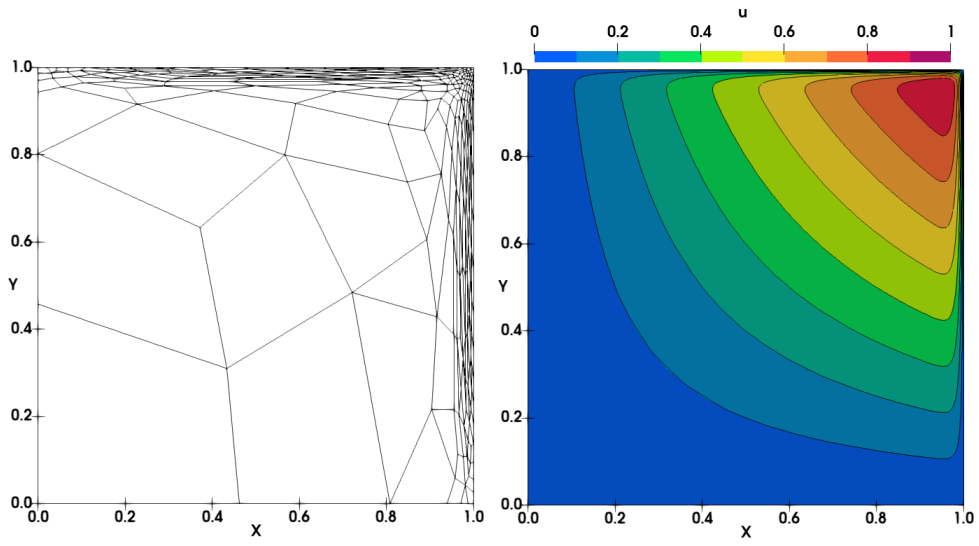

(a) (b)

Figure 3: Scalar Advection - Diffusion test case: (a) Adapted quad-dominant mesh ($n_h = 276$, $DoF = 1479$, $p = 2$), (b) Contour plot of the numerical solution, $||u - u_h||_{L_2(\Omega)} = 4.03 \times 10^{-5}$

Fig. 4 shows the variation of L_2-norm of exact error w.r.t. indicative mesh size ($h \equiv 1/\sqrt{DoF}$) for $p = 2$, 3 and 4. As expected, increasing polynomial order results in a lower error at the same DoF. The figure shows that the error for adapted mesh is much lower than for uniform refinement case for $p = 2$. Many sub-iterations for mesh adaptation are performed for a given N. When the L_2-norm of exact error between three subsequent sub-iterations did not vary much, N is increased by 30%, and the same process is repeated. Thus, all the data points plotted in Fig. 4 correspond to the last adapted mesh for a given N, except the very first data point, which corresponds to the error on an initial coarse mesh. A mesh

adaptation cycle typically consists of many such sub-iterations at increasing values of N. As seen from the figure, we achieve early optimum order of error convergence of order $p+1$, even on large mesh sizes h, because of the equidistribution of error across all the mesh elements. Fig. 5 shows the variation of L_2-norm of exact error over all the mesh elements (κ). The error varies fourteen orders of magnitude across the elements of the initial mesh. The lower errors ($\sim 10^{-16}$) correspond to the elements at the domain's bottom-left corner. The higher errors ($\sim 10^{-2}$) correspond to the elements in the top-right corner of the domain where the solution exhibits high variations. As the mesh adaptation cycle proceeds, the elements are refined and arranged in an anisotropic manner in the top-right corner of the domain at the expense of coarsening the elements elsewhere. This results in an almost equidistribution of the errors across the domain in just five adaptations. Thus, the mesh adaptation framework results in the most optimum mesh for a given complexity N.

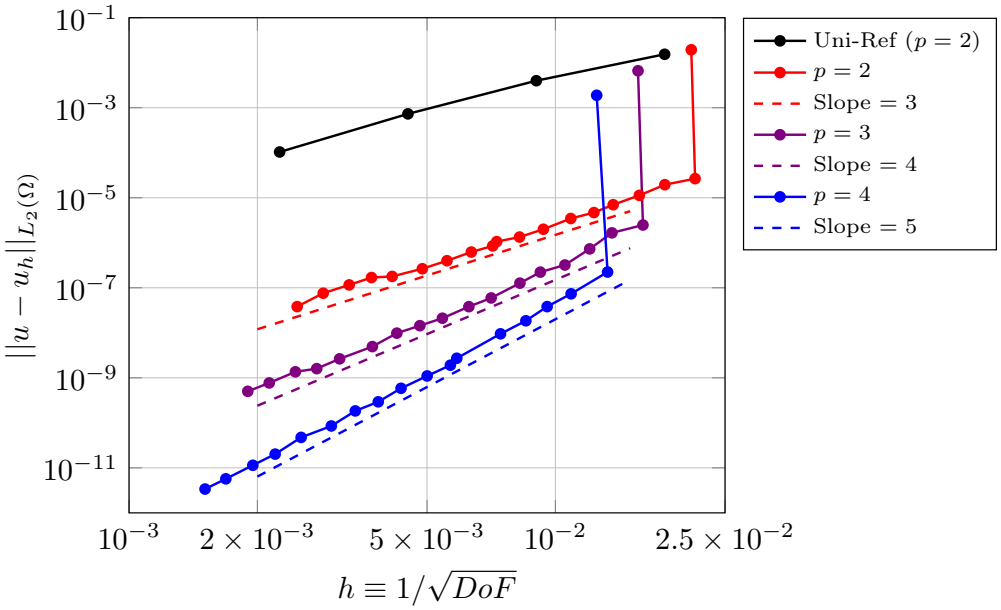

Figure 4: Scalar Advection - Diffusion test case: convergence of L_2-norm of exact error w.r.t indicative mesh size (h) for various polynomial orders

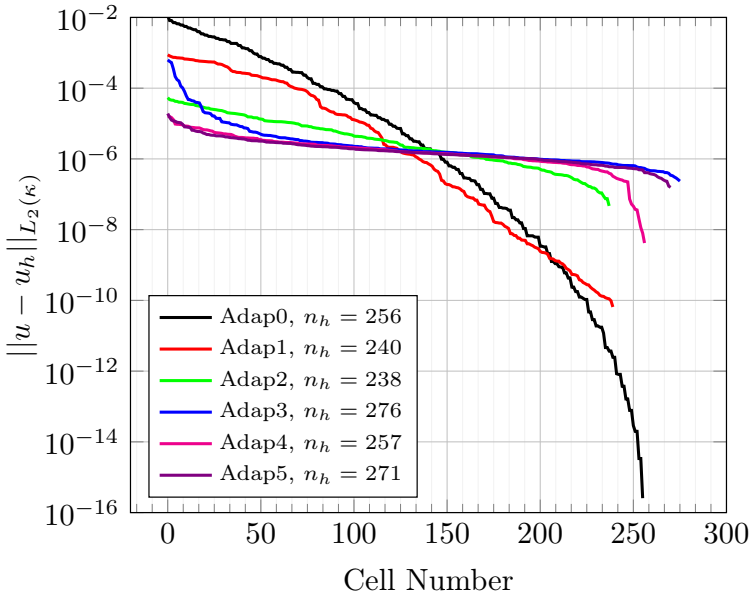

Figure 5: Scalar Advection - Diffusion test case: equidistribution of L_2-norm of elemental errors for various adaptation cycles for $p = 2$ at a given complexity N

3.2 Turbulent flow over a flat plate

We consider a subsonic flow past a zero pressure gradient flat plate with freestream Mach number of $M_\infty = 0.2$ and Reynolds number $Re = 5 \times 10^6$ based on unit length. The length of the plate is two units from $x = 0$ to $x = 2$. This test case is well documented on NASA's Turbulence Modeling Resource (TMR) website. Riemann invariant inflow and outflow boundary conditions are prescribed in the left and right boundaries. The top boundary is considered as far-field. The bottom boundary initially consists of a symmetry condition followed by an adiabatic wall from $x = 0$ to $x = 2$. One-equation Spalart-Allmaras (SA) model is used for turbulence modeling with the SA working variable $\nu/\nu_\infty = 3$.

We start from a coarse mesh with 311 elements, $p = 2$ and $DoF = 1689$. Fig. 6 shows the mach contour on an initial mesh with an unresolved boundary layer. The mesh is adapted multiple times based on the interpolation error in Mach number, and we get a final adapted quad-dominant mesh with 8235 elements and $DoF = 41187$. Fig. 7 shows the adapted mesh, having a sufficiently resolved boundary layer and leading edge singularity at $x = 0$. From the zoomed-in mesh, it is seen that elements are highly anisotropic within the boundary layer and coarse and isotropic elsewhere.

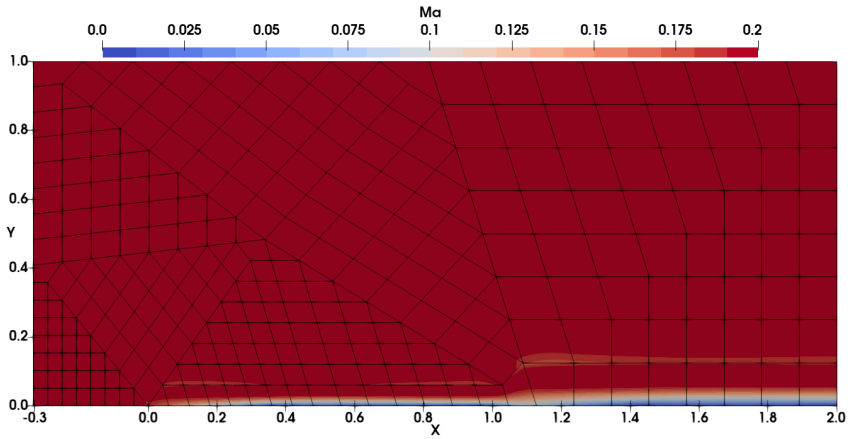

Figure 6: Turbulent flow over a flat plate: initial mesh and Mach contour ($n_h = 311$, $DoF = 1689$, $p = 2$)

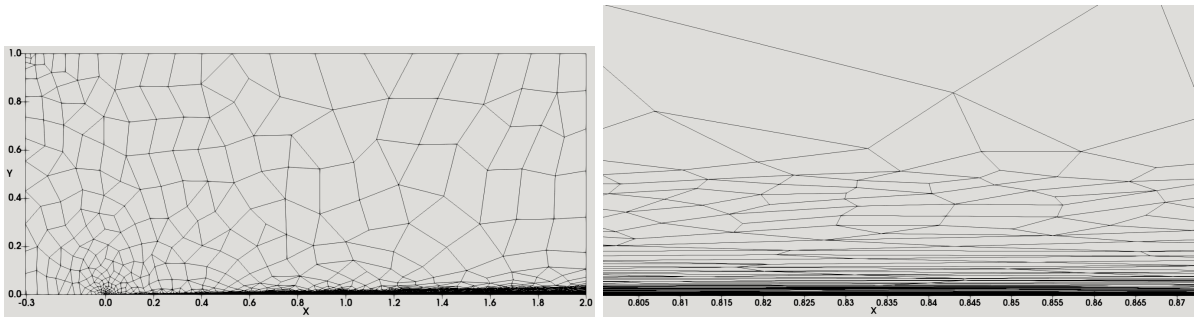

(a) (b)

Figure 7: Turbulent flow over a flat plate: (a) Adapted quad-dominant mesh ($n_h = 8235$, $DoF = 41187$, $p = 2$), (b) zoomed-in adapted mesh

We compare the skin friction coefficient (C_f) that is calculated on an adapted mesh with the results from two finite volume solvers, CFL3D and FUN3D, available on the TMR website. Fig. 8 shows the variation of C_f over the flat plate for the adapted mesh and results from CFL3D and FUN3D. The adapted quad-dominant mesh has $DoF = 41187$, while the reference data from CFL3D and FUN3D has $DoF = 208896$. All three results nicely overlap each other, signifying that the adapted mesh achieves almost similar boundary layer resolution with much less DoF. Drag convergence study was performed on the adapted meshes, and the results were compared with that of CFL3D and FUN3D. Fig. 9 shows the convergence of C_d w.r.t DoF. It is observed that for CFL3D, drag convergence is achieved at around 200000 DoF, while with mesh adaptation, drag convergence is achieved much earlier (around 22000 DoF), which is a huge advantage in terms of computational cost.

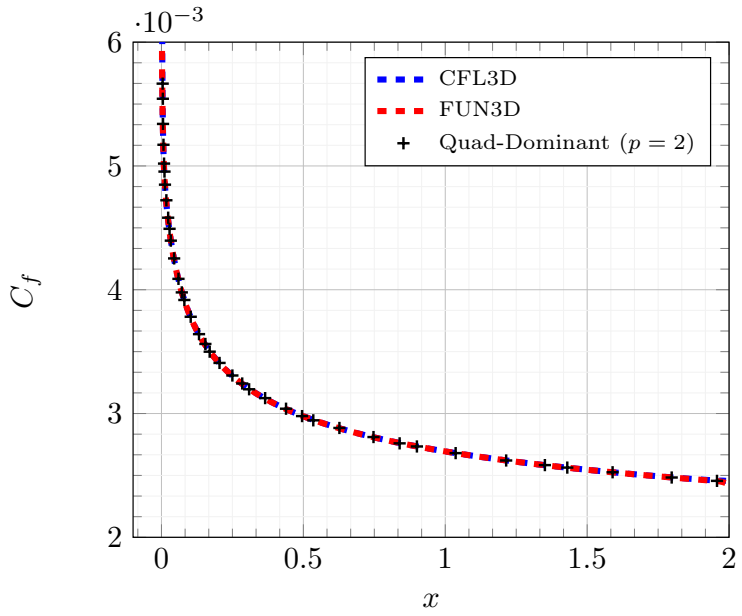

Figure 8: Turbulent flow over a flat plate: variation of skin friction coefficient (C_f) over the flat plate. For adapted quad-dominant mesh $n_h = 8235$, $DoF = 41187$, and $p = 2$

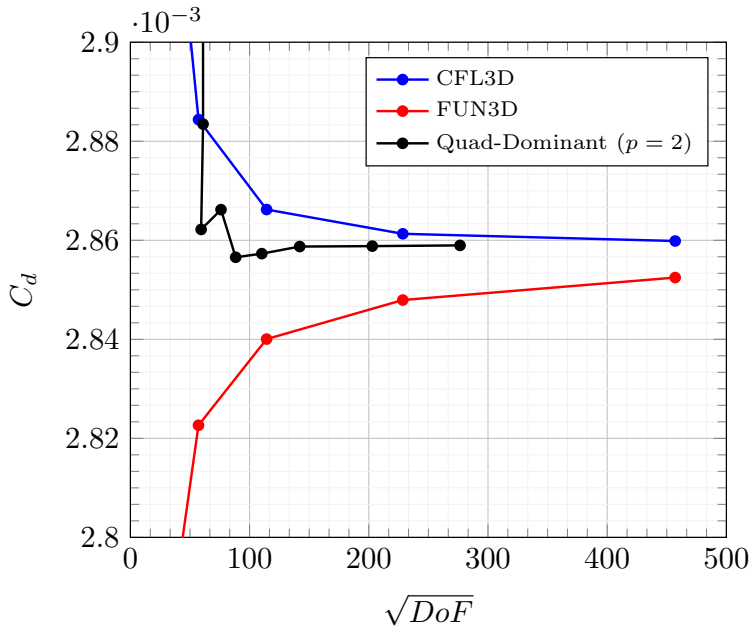

Figure 9: Turbulent flow over a flat plate: convergence of drag coefficient (C_d)

4 Conclusion and Future Work

An extension of metric field based mesh adaptation to quad-dominant meshes for high-order DG methods has been presented. The adaptation methodology relies on analytical optimization, requiring only the desired number of degrees of freedom to generate an adapted mesh. Blossom-Quad algorithm has been used to get optimum quads by recombining triangles. The methodology is tested for various flow scenarios.

For the scalar advection-diffusion test case, mesh adaptation achieves optimum order of error convergence even on coarse meshes. This is because the mesh adaptation algorithm drives the meshes towards the one with the errors equidistributed across the mesh elements, giving us the most optimal mesh for a given complexity N. For turbulent flow over a flat plate, mesh adaptation achieved drag convergence at a much lower DoF compared to the results of FUN3D and CFL3D.

As a future work, we plan to extend the current framework to adjoint and hp-mesh adaptation and couple it with quasi-structured meshes to get almost right-angled adapted quads within the boundary layer and around shocks.

References

[1] Jeffrey P Slotnick, Abdollah Khodadoust, Juan Alonso, David Darmofal, William Gropp, Elizabeth Lurie, and Dimitri J Mavriplis. Cfd vision 2030 study: a path to revolutionary computational aerosciences. Technical report, 2014.

[2] GARY WARREN, Wit Anderson, JAMES THOMAS, and Sherrie Krist. Grid convergence for adaptive methods. In *10th Computational Fluid Dynamics Conference*, page 1592, 1991.

[3] Pascal-Jean Frey and Frédéric Alauzet. Anisotropic mesh adaptation for cfd computations. *Computer methods in applied mechanics and engineering*, 194(48-49):5068–5082, 2005.

[4] Frédéric Hecht, Bijan Mohammadi, F Hecht, and B Mohammadi. Mesh adaption by metric control for multi-scale phenomena and turbulence. In *35th Aerospace Sciences Meeting and Exhibit*, page 859, 1997.

[5] Aravind Balan, Michael A Park, Stephen Wood, and William K Anderson. Verification of anisotropic mesh adaptation for complex aerospace applications. In *AIAA scitech 2020 forum*, page 0675, 2020.

[6] Adrien Loseille and Frédéric Alauzet. Continuous mesh framework part i: well-posed continuous interpolation error. *SIAM Journal on Numerical Analysis*, 49(1):38–60, 2011.

[7] Adrien Loseille and Frédéric Alauzet. Continuous mesh framework part ii: validations and applications. *SIAM Journal on Numerical Analysis*, 49(1):61–86, 2011.

[8] Krzysztof J Fidkowski and David L Darmofal. Review of output-based error estimation and mesh adaptation in computational fluid dynamics. *AIAA journal*, 49(4):673–694, 2011.

[9] Adrien Loseille, Alain Dervieux, and Frédéric Alauzet. Fully anisotropic goal-oriented mesh adaptation for 3d steady euler equations. *Journal of computational physics*, 229(8):2866–2897, 2010.

[10] Anca Belme, Frédéric Alauzet, and Alain Dervieux. An a priori anisotropic goal-oriented error estimate for viscous compressible flow and application to mesh adaptation. *Journal of Computational Physics*, 376:1051–1088, 2019.

[11] Frederic Alauzet and Loïc Frazza. 3d rans anisotropic mesh adaptation on the high-lift version of nasa's common research model (hl-crm). In *AIAA Aviation 2019 Forum*, page 2947, 2019.

[12] Frédéric Alauzet and Loïc Frazza. Feature-based and goal-oriented anisotropic mesh adaptation for rans applications in aeronautics and aerospace. *Journal of Computational Physics*, 439:110340, 2021.

[13] Vít Dolejší. Anisotropic hp-adaptive method based on interpolation error estimates in the lq-norm. *Applied Numerical Mathematics*, 82:80–114, 2014.

[14] Aravind Balan, Michael Woopen, and Georg May. Adjoint-based hp-adaptivity on anisotropic meshes for high-order compressible flow simulations. *Computers & Fluids*, 139:47–67, 2016.

[15] Ajay Rangarajan, Aravind Balan, and Georg May. Mesh optimization for discontinuous galerkin methods using a continuous mesh model. *AIAA Journal*, 56(10):4060–4073, 2018.

[16] Vít Dolejší, Georg May, and Ajay Rangarajan. A continuous hp-mesh model for adaptive discontinuous galerkin schemes. *Applied Numerical Mathematics*, 124:1–21, 2018.

[17] Ajay Mandyam Rangarajan, Ankit Chakraborty, Georg May, and Vit Dolejsi. A continuous-mesh optimization technique for piecewise polynomial approximation on tetrahedral grids. In *2018 Fluid Dynamics Conference*, page 3246, 2018.

[18] Ajay Rangarajan, Georg May, and Vit Dolejsi. Adjoint-based anisotropic hp-adaptation for discontinuous galerkin methods using a continuous mesh model. *Journal of Computational Physics*, 409:109321, 2020.

[19] Ajay Mandyam Rangarajan, Ankit Chakraborthy, and Georg May. A goal oriented optimization technique for tetrahedral grids using a continuous-mesh model. In *AIAA Scitech 2019 Forum*, page 0349, 2019.

[20] Aravind Balan, Michael A Park, Stephen L Wood, W Kyle Anderson, Ajay Rangarajan, Devina P Sanjaya, and Georg May. A review and comparison of error estimators for anisotropic mesh adaptation for flow simulations. *Computers & Fluids*, 234:105259, 2022.

[21] D Marcum and F Alauzet. 3d metric-aligned and orthogonal solution adaptive mesh generation. *Procedia engineering*, 203:78–90, 2017.

[22] Graham Candler, Michael Barnhardt, Travis Drayna, Ioannis Nompelis, David Peterson, and Pramod Subbareddy. Unstructured grid approaches for accurate aeroheating simulations. In *18th AIAA computational fluid dynamics conference*, page 3959, 2007.

[23] Adrien Loseille. Metric-orthogonal anisotropic mesh generation. *Procedia Engineering*, 82:403–415, 2014.

[24] Adrien Loseille, David L Marcum, and Frederic Alauzet. Alignment and orthogonality in anisotropic metric-based mesh adaptation. In *53rd AIAA Aerospace Sciences Meeting*, page 0915, 2015.

[25] Bruno Lévy and Yang Liu. L p centroidal voronoi tessellation and its applications. *ACM Transactions on Graphics (TOG)*, 29(4):1–11, 2010.

[26] Dirk Ekelschot, Marco Ceze, Anirban Garai, and Scott M Murman. Robust metric aligned quad-dominant meshing using lp centroidal voronoi tessellation. In *2018 AIAA Aerospace Sciences Meeting*, page 1501, 2018.

[27] Keigan MacLean and Siva Nadarajah. Anisotropic mesh generation and adaptation for quads using the lp-cvt method. *Journal of Computational Physics*, 470:111578, 2022.

[28] J-F Remacle, Jonathan Lambrechts, Bruno Seny, Emilie Marchandise, Amaury Johnen, and C Geuzainet. Blossom-quad: A non-uniform quadrilateral mesh generator using a minimum-cost perfect-matching algorithm. *International journal for numerical methods in engineering*, 89(9):1102–1119, 2012.

[29] Frédéric Hecht. Bamg: bidimensional anisotropic mesh generator. *User Guide. INRIA, Rocquencourt*, 17, 1998.

[30] Michael Woopen, Aravind Balan, and Georg May. A unifying computational framework for adaptive high-order finite element methods. In *22nd AIAA Computational Fluid Dynamics Conference*, page 2601, 2015.

[31] Michael Woopen, Aravind Balan, and Georg May. A hybridized discontinuous galerkin method for three-dimensional compressible flow problems. In *52nd Aerospace Sciences Meeting*, page 0938, 2014.